9. Kinahan PE, Rogers JG. Analytic 3D image reconstruction using all detected events. *IEEE TNS* 1989;36:964–968.
10. Logan J, Fowler JS, Volkow ND, et al. Graphical Analysis of reversible radioligand binding from time-activity measurements applied to [N-^{11}C-methyl-(-)-cocaine PET studies in human subjects. *J Cereb Blood Flow Metab* 1990;10:740–747.
11. Logan J, Fowler JS, Volkow ND, Wang G-J, Ding Y-S, Alexoff DL. Distribution volume ratios without blood sampling from graphical analysis of PET data. *JCBF* 1996;16:834–840.
12. Phelps ME Huang SC, Hoffman EJ, Selinss C, Sokoloff L, Kuhl DE. Tomographic measurement of local cerebral glucose metabolic rate in humans with ^{18}F-2-fluoro-2-deoxy-D-glucose:validation of method. *Ann Neurol* 1979;6:371–388.
13. Spinks TJ, Jones T, Bailey DJ, et al. Physical performance of a positron tomograph for brain imaging with retractable septa. *Phys Med Biol* 1992;37:8: 1637–1655.
14. Ravert HT, Wilson AA, Dannals RF, Wong DF, Wagner HN. Radiosynthesis of a selective dopamine D-1 receptor antagonist: R(+)-7chloro-8-hydroxy-3-[^{11}C]methyl-1-phenyl-1,2,3,4,5-tetardhydro-1H-3-benzazepine ([^{11}C]SCH 23390). *Appl Radiat Isot* 1987;38:305–306.

15. Kilboum, Lee L, Vander Borght T, Jewett D, Frey K. Binding of α-dihydrotetrabena-zine to the vesicular monoamine transporter is stereospecific. *Eur J Pharmacol* 1995;278:249–252.
16. Chan GL-Y, Holden JE, Stoessl J et al. Reproducibility of [^{11}C]SCH 23390 PET in normal human subjects. *J Nucl Med* 1998;39:792–797.
17. Frey KA, Koeppe RA, Kilboum MR. Presynaptic monoaminergic vesicles in Parkinson's disease and normal aging. *Ann Neurol* 1996;40:873–884.
18. Fleiss JL. *The design and analysis of clinical experiment.* New York: John Wiley & Sons: 1986:263–290.
19. Scheffe H. *The analysis of variance.* New York: John Wiley & Sons;1959:221–260.
20. Trebossen R, Bendriem B, Fontaine A et al. Quantitation of the [^{18}F]fluorodopa uptake in the human striata in 3D PET with the ETM scatter correction. *Quantification of brain using PET.* San Diego: Academic Press; 1996:88–92.
21. Townsend DW, Price JC, Lopresti BJ et al. Scatter correction for brain receptor quantitation in 3D PET. *Quantification of brain using PET.* Academic Press; 1996:76–81.

Significance of Nonuniform Attenuation Correction in Quantitative Brain SPECT Imaging

Nallakkandi Rajeevan, I. George Zubal, S. Quinn Ramsby, Sami S. Zoghbi, John Seibyl and Robert B. Innis

Departments of Diagnostic Radiology and Psychiatry, Yale University School of Medicine, New Haven; and Veterans Affairs Connecticut, New Haven, Connecticut

The purposes of this study were to develop a method for nonuniform attenuation correction of ^{123}I emission brain images based on transmission imaging with a longer-lived isotope (i.e., ^{57}Co) and to evaluate the relative improvement in quantitative SPECT images achieved with nonuniform attenuation correction. **Methods:** Emission and transmission SPECT scans were acquired on three different sets of studies: a heterogeneous brain phantom filled with ^{123}I to simulate the distribution of dopamine transporters labeled with 2β-carbomethoxy-3β-(4-^{123}I-iodophenyl)tropane (^{123}I-β-CIT); nine healthy human control subjects who underwent transmission scanning using two separate line sources (^{57}Co and ^{123}I); and a set of eight patients with Parkinson's disease and five healthy control subjects who received both emission and transmission scans after injection of ^{123}I-β-CIT. Attenuation maps were reconstructed using a Bayesian transmission reconstruction algorithm, and attenuation correction was performed using Chang's postprocessing method. The spatial distribution of errors within the brain was obtained from attenuation correction factors computed from uniform and nonuniform attenuation maps and was visualized on a pixel-by-pixel basis as an error image. **Results:** For the heterogeneous brain phantom, the uniform attenuation correction had errors of 2%–6.5% for regions corresponding to striatum and background, whereas nonuniform attenuation correction was within 1%. Analysis of ^{123}I transmission images of the nine healthy human control subjects showed differences between uniform and nonuniform attenuation correction to be in the range of 6.4%–16.0% for brain regions of interest (ROIs). The human control subjects who received transmission scans only were used to generate a curvilinear function to convert ^{57}Co attenuation values into those for ^{123}I, based on a pixel-by-pixel comparison of two coregistered transmission images for each subject. These values were applied to the group of patients and healthy control subjects who received transmission ^{57}Co scans and emission ^{123}I scans after injection of ^{123}I-β-CIT. In comparison to nonuniform attenuation correction as the gold standard, uniform attenuation with the ellipse drawn around the transmission image caused an ~5% error, whereas placement of the ellipse around the emission image caused a 15% error. **Conclusion:** Nonuniform attenuation correction allowed a moderate improvement in the measurement of absolute activity in individual brain ROIs. When images were analyzed as target-to-background activity ratios, as is commonly performed with ^{123}I-β-CIT, these outcome measures showed only small differences when Parkinson's disease patients and healthy control subjects were compared using nonuniform, uniform or even no attenuation correction.

Key Words: quantitative SPECT; nonuniform attenuation correction; brain imaging

J Nucl Med 1998; 39:1719–1726

The importance of nonuniform attenuation correction in SPECT imaging of highly heterogeneous sections of the body, like the thorax, is well recognized (*1*). However, its significance in quantitative brain SPECT imaging has not been so well documented. Routine clinical brain SPECT imaging still uses uniform attenuation correction, assuming that the head has homogeneous attenuation properties and elliptical cross-sections. Here, we examine the heterogeneity of the head and analyze the significance of nonuniform attenuation correction in quantifying radioligand distribution in the brain using SPECT imaging.

Various methods for attenuation correction in SPECT have been proposed. These methods can be classified as:

1. Object space postprocessing methods (*2*);
2. Attenuation-weighted backprojection (*3,4*); and
3. Iterative projection-backprojection methods (*5–8*).

In postprocessing methods, such as Chang's algorithm (*2*), an attenuation correction factor for each voxel in the object is first computed from a map of the attenuation coefficients of the object. These correction factors are then applied to the reconstructed emission image. In the attenuation-weighted backprojection methods, the image reconstruction filter (i.e., ramp filter multiplied by a window function) is modified in such a way that the filter is a function of the constant attenuation coefficient for the object. In iterative methods, pseudoprojections of an estimated emission image through the attenuation

map are first computed. A correction to the emission image is applied based on the difference in the pseudoprojections and the actual measurement projection data. This process of pseudoprojection and object correction is iterated until a suitable convergence is obtained. The iterative methods are computationally very expensive, so they have limited use in present day routine clinical applications. Here, we have used the postprocessing method proposed as Chang's algorithm to analyze the significance of nonuniform attenuation correction in quantitative brain SPECT imaging. A similar analysis in PET using a hybrid method for attenuation correction has been reported (9). The effect of attenuation due to the skull in brain SPECT was studied previously (10,11).

An essential requirement in applying nonuniform attenuation correction is the availability of a map of the attenuation coefficients of the object. Such an attenuation map in SPECT can be obtained by transmission imaging of the object using an external line source of radiation. Methods of doing transmission imaging, simultaneously (8,12) or sequentially (13) with the emission scan, on three-head SPECT systems are now available. To avoid cross-contamination, it is advantageous for the photon energy from the transmission source to be different from that of the emission photons from the radioligand. This study focuses on SPECT imaging with ^{123}I-labeled ligands using [57]Co for transmission imaging.

This study used both phantom and human data, which reflected the activity distribution of 2β-carbomethoxy-3β-(4-^{123}I-iodophenyl)tropane (^{123}I-β-CIT) in striatal or midbrain regions. The radioligand ^{123}I-β-CIT is an analog of cocaine and labels the dopamine transporter, a molecule on the terminal projections of dopamine-containing neurons with cell bodies in the substantia nigra. The symptoms of idiopathic Parkinson's disease are caused by a degeneration of dopamine-containing neurons in the substantia nigra, as well as their terminal projections to the striata. Thus, the dopamine transporter is a marker for Parkinson's disease because its loss would be expected to mirror the loss of dopaminergic innervation of the striatum. In fact, ^{123}I-β-CIT SPECT imaging has been shown by several groups to provide early diagnostic information in idiopathic Parkinson's disease (14). The midbrain uptake of ^{123}I-β-CIT has been shown to largely reflect seratonin transporters (15). The images of striata and midbrain ^{123}I-β-CIT activity are typically quantified either as percentage injected dose (%ID) per region of interest (ROI) or as a target-to-background activity ratio (e.g., striatum-to-occipital ratio, -1). The effects of uniform and nonuniform attenuation correction were assessed on both these imaging outcome measures.

MATERIALS AND METHODS

Data Acquisition

Both emission and transmission data were collected on a PRISM3000 triple-head SPECT system equipped with the STEP® (simultaneous transmission and emission protocol) attachment for transmission imaging. The transmission line source was positioned at the focal line of the fanbeam collimator on head 3. To compare attenuation of [57]Co with that of ^{123}I, transmission scans were taken on nine healthy human control subjects using a 10-mCi [57]Co and a 6-mCi ^{123}I transmission line source. For the [57]Co transmission scan, an energy window of 15% of the primary photopeak (122 keV) was used. For ^{123}I transmission scans, the energy window used was 20% of the primary photopeak (159 keV) of [123]I. For the transmission scans, data were collected for 15 min in 120 equiangular projections in 360°. The emission photons from the ^{123}I source distribution in the object were collected in an energy

window of 20% centered at 159 keV for 24 min from 120 equiangular projections in 360°.

The simultaneous collection of emission and transmission photons in [57]Co and ^{123}I windows, respectively, resulted in excessive contamination of ^{123}I emission data by spillover of photons from [57]Co transmission source. In contrast, the counts from the [57]Co transmission source were of the order of 1 million cpm, much greater than the counts (of the order of 10000 cpm) from the ^{123}I emissions from within the object detected in the [57]Co window. This small spillover from the ^{123}I emissions was removed by subtracting the average of ^{123}I emissions detected in [57]Co window on heads 1 and 2. To eliminate [57]Co counts in the ^{123}I window, the transmission and emission scans were taken sequentially, making sure that the patient had not moved between these scans. In summary, the high activity of the [57]Co line source allowed transmission images to be acquired in the presence of ^{123}I activity within the object, but emission images had to be acquired in the absence of the transmission source.

Reconstruction of the Attenuation Map

The attenuation map of the head along with the head-holder was reconstructed from transmission and flood data using a Bayesian algorithm with a smoothing Gibbs prior, which is a modification to the maximum likelihood algorithm for transmission reconstruction proposed by Lange and Carson (16). This algorithm is based on the assumption that both incident flood data (f = {f_j,j = 1,M}) and transmission data (y = {y_j,j = 1,M}, where M is the number of measurements) are samples from Poisson processes. This Bayesian algorithm assumes that the mean (μ) of the regional attenuation coefficient can be modeled as a Gibbs random field, given by:

$$P(\mu) = \frac{1}{Z} e^{-U(\mu)/\beta.}$$ Eq. 1

Here, $U(\mu)$ is the energy of the configuration μ, and Z is a normalization factor [details on incorporating Gibbs smoothing priors in Bayesian image reconstruction have been reported previously (17)]. In each iteration, the new estimate μ_i^{n+1} of the attenuation coefficient at the spatial position (pixel) i is computed from the transmission data y and the flood data f as:

$$\mu_i^{n+1} = \mu_i^n + \Delta\mu_i^n \frac{\Sigma_j l_{ij}[f_j exp(\Sigma_i l_{ij}\mu_i^n) - y_j] - \beta \frac{\partial U(\mu^n)}{\partial \mu_j}}{\Sigma_j l_{ij}\Sigma_i l_{ij}\mu_i^n f_j exp(\Sigma_i l_{ij}\mu_i^n)}$$ Eq. 2

where l_{ij} is the line intersect of ray j with pixel i. Δ is a relaxation parameter, and β controls the influence of priors in the reconstruction.

Conversion from Cobalt-57 Attenuation Map to Iodine-123 Map

Conversion of [57]Co attenuation map to that for ^{123}I was performed using an experimentally obtained functional relationship between attenuation coefficients for [57]Co and ^{123}I gamma rays. To obtain this function, transmission scans of the head were taken on a set of nine human control subjects (five men and four women) with both [57]Co and ^{123}I sources, as described above. The reconstructed [57]Co and ^{123}I attenuation maps were coregistered using the program ANALYZE (CNSoftware, Rochester, MN). The attenuation coefficient in each pixel of the [57]Co attenuation map was compared with that in the corresponding pixel of the ^{123}I attenuation map. A two-dimensional histogram of [57]Co versus ^{123}I attenuation coefficients was generated, and a functional relationship between [57]Co and ^{123}I attenuation coefficients was obtained by least squares fitting.
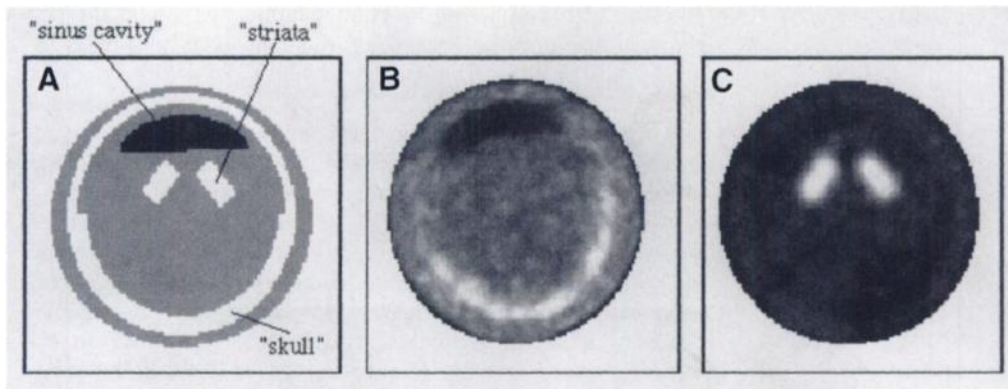
FIGURE 1. Cross-section of head phantom consisting of left and right striatum, sinus cavity and skull. (A) Schematic diagram of cross-section through striata, showing both emission and attenuation regions. Also shown are cross-sections of (B) attenuation map and (C) emission image, through striata of phantom.

Uniform and Nonuniform Attenuation Correction

In both the uniform and nonuniform cases, the attenuation correction was applied using Chang's first-order algorithm. For M projections, this algorithm first computes an estimate of the mean attenuation (A$_i$) experienced by photons emitted in a given voxel(i) as:

$$A_i = \frac{1}{M} \sum_j \exp\left(- \sum_{i'} l_{i'j}\mu_{i'}\right). \qquad \text{Eq. 3}$$

In the case of uniform attenuation, the coefficients μ_i are constant in all the voxels. In the first-order Chang attenuation correction method (2), the inverse of this average attenuation was used as the correction factor (C$_i$) to be applied on the emission image. That is, the correction factors (C$_i$) given by:

$$C_i = \frac{1}{\frac{1}{M} \sum_j \exp\left(- \sum_{i'} l_{i'j}\mu_{i'}\right)}, \qquad \text{Eq. 4}$$

were applied on the filtered backprojection reconstructed emission image.

To obtain the mean coefficient for uniform attenuation correction, ellipses were drawn around the object, and integrated attenuation and path length were computed along all projection rays and angles. The uniform linear attenuation coefficient was then calculated as:

$$\mu_{av} = \frac{\sum_j \sum_i l_{ij}\mu_i}{\sum_j l_j}, \qquad \text{Eq. 5}$$

where the numerator gives the total attenuation and the denominator gives the total path length through the attenuation map.

Scatter Correction

Compensation for detected scatter photons in the data was achieved by scaling down the attenuation coefficient by an experimentally determined factor. A realistic human head phantom (anthropomorphic striatal phantom; Radiologic Support Devices, Long Beach, CA) was used to determine this scaling factor. This phantom was built in a human skull with a plastic shell insert of 1300-ml volume to simulate the brain. The average attenuation coefficient for ^{123}I radiation for this phantom was 0.136 cm^{-1}, which was very similar to that obtained for the human head (0.137 cm^{-1}), measured using the same method by transmission imaging in nine healthy human control subjects.

The brain cavity was filled with a uniform solution of [123]I (0.48 μCi/cm^3), and the emission image was reconstructed using filtered backprojection without applying any attenuation correction. Several trial scaling factors (range 0.5–1.0) were applied to the attenuation map, and nonuniform attenuation correction was applied to the emission image. By examining the profile through the

center of the attenuation-corrected emission image, the scaling factor for scatter was adjusted such that the emission image, after attenuation correction using a scaled attenuation map, had uniform activity across the reconstructed image. The scatter scaling determined in this way (0.78) was multiplied subsequently on a pixel-by-pixel basis to the μ values in the uniform and nonuniform images. The emission images of the anthropomorphic phantom were used then to measure sensitivity (cpm/μCi).

Heterogeneous Phantom

A heterogeneous phantom was constructed in a cylinder (20 cm diameter × 20 cm length). To simulate the left and right striata, two small 5-ml cylinders were used (Fig. 1). A 4-mm-thick aluminum sheet, bent in the shape of a semicircular cylinder, was attached in place of the rear part of the skull, and a similar 2-mm-thick aluminum semicircular cylinder was used as the front of the skull. To simulate the sinus cavities, a block of styrofoam was used. The region surrounding these inserts was filled with radioactive solution, to reflect the background activity in the brain.

Both transmission (using a 10-mCi ^{57}Co line source) and emission data were collected for a duration of 15 min. The emission image was reconstructed using filtered backprojection with a Butterworth prefilter of order 10 and cutoff 0.24 of the Nyquist frequency. The measured counts in a large striatal ROI was assumed to be the sum of the counts in the striata and the background activity in the ROI outside the striata. The counts in the striata were then obtained by subtracting the background counts from the total counts in the ROI.

Human Control Subjects

Nine healthy human control subjects (5 men, 4 women; mean age 41 ± 9 yr; these and subsequent data expressed as mean ± s.d.) were scanned in the transmission only imaging experiment, with no injected activity. Each received two 15-min transmission scans (a 10-mCi ^{57}Co and a 6-mCi ^{123}I line source).

For the experiments with emission (24 min) and transmission imaging (15-min ^{57}Co scan), five healthy control subjects (48 ± 17 yr) and eight patients (59 ± 14 yr) with idiopathic Parkinson's disease (Hoehn–Yahr Stage, 2.0 ± 0.5) were scanned. These Parkinson's disease patients were evaluated using the Unified Parkinson's Disease Rating Scale after an overnight withdrawal of medication (18) and had a total symptom score of 32 ± 11. Control subjects received 6.1 ± 0.1 mCi of ^{123}I-β-CIT and were scanned 24 hr postinjection.

Region of Interest Analysis

For the control subjects who had only transmission scans, anatomical landmarks were identified in each subject's transmission image. The thalamic slices, which included the ROIs for striata, thalamus, frontal, occipital and temporal–parietal, were identified using the approximately largest anterior–posterior dimension from frontal pole to occipital pole as the central
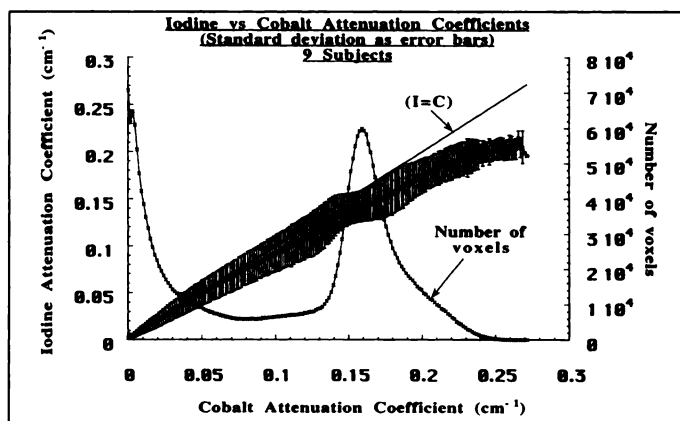
FIGURE 2. Functional relation between attenuation coefficients for gamma rays from ^{123}I and [57]Co. This curve was obtained by least squares fitting of two-dimensional histogram of attenuation maps. Curve shows mean ± s.d. of iodine attenuation coefficient for each cobalt attenuation coefficient value. Straight line (I = C) shows hypothetical relationship if attenuation of ^{123}I were equal to that of [57]Co. A second experimental curve (×) plots total number of voxels in transmission image of head for each cobalt attenuation coefficient.

slice through the region. Seven contiguous transaxial slices around this central slice were selected for drawing these ROIs. Similarly, the pontine slices were selected by identifying the horizontal section midway between the superior and inferior extent of petrous sinus. With this section as the reference, five slices were selected around it, and ROIs for cerebellum and pones were drawn. For drawing the midbrain ROI, four slices immediately above the pontine slices were used. For subjects who had both emission and transmission scans, ROIs for striata, midbrain and thalamus were visually identified in the emission image, as described previously (*14*).

RESULTS

Transmission Imaging

The [57]Co and ^{123}I attenuation maps reconstructed from transmission data taken on humans were used to generate the function relating attenuation coefficients for [57]Co and ^{123}I gamma rays in the human head. This function was generated by least squares fitting of the data in three distinct regions corresponding to the [57]Co attenuation values of 0–0.13, 0.13–0.15 and 0.15–3.0 cm^{-1} (Fig. 2). As expected, the majority of the voxels had attenuation coefficient values of ~0.15 cm^{-1}, which is the accepted coefficient for tissue or water. The [57]Co versus ^{123}I plot of every subject demonstrated an upward deflection near 0.15 cm^{-1} of [57]Co attenuation values. To identify which pixels tended to cause this upward deflection, we viewed those pixels with [57]Co values ranging from 0.13 cm^{-1} to 0.15 cm^{-1} and with ^{123}I values falling in the upper portion of the curve. Most of these pixels fell discretely along the interface of bone and tissue. Thus, the upward deflection was caused, in part, by the nonlinearity of ratio of [57]Co to ^{123}I attenuation values in regions with partial volume effects from tissues of differing densities.

The attenuation value used for uniform attenuation correction was calculated as the mean value from the transmission image from either all slices of a single image or from all slices of the entire group (see below). Thus, the average correction factor for the entire head calculated with uniform attenuation correction should be equal to that from nonuniform attenuation correction. We confirmed this expectation in one subject by using a large ROI encompassing the entire head in all transaxial slices.

To analyze the spatial variability of errors in quantitation with different methods, correction factors were generated using

both uniform and nonuniform attenuation maps, and the percentage difference between them was displayed on a pixel-by-pixel basis (Fig. 3). The spatial variability of errors in attenuation correction is evident from this image. When compared to the nonuniform method, uniform attenuation undercorrected regions closer to the back of the skull. In contrast, regions closer to the sinus cavities were overcorrected with uniform attenuation correction. For example, the occipital region was undercorrected (−10.6%) and the ethmoid sinus was overcorrected (45%) with uniform attenuation (Table 1). The average attenuation value varied significantly for different cross-sectional slices in a single individual and between subjects. In our experiments, the average attenuation was 0.139 ± 0.004 cm^{-1} for the slices through the striatal region but only 0.130 ± 0.003 cm^{-1} (n = 9 subjects) for the slices through the cerebellum. Similarly, the average uniform attenuation coefficient of all slices for each subject varied from 0.134 to 0.142 cm^{-1}, with a mean value of 0.138 ± 0.003 cm^{-1}. Uniform attenuation correction uses a single μ value for the entire group. As would be predicted, the variability (measured as s.d.) of the uniform-to-nonuniform attenuation correction ratio was increased when a single population μ value was used for uniform attenuation correction compared to an individually based μ value (Table 1).

Phantom Studies with Emission and Transmission Imaging

The recovered activity in the left and right striata and background in the reconstructed images with uniform and nonuniform attenuation correction and their percentage errors are shown in Table 2. The percentage error in recovered activity using uniform attenuation correction was ~6%, whereas that for nonuniform attenuation correction was within 1% of the true activity.

Effect of Head-Holder

Attenuation correction factors were generated from the transmission image of the anthropomorphic phantom with and without the head-holder and then applied to the emission image. The effect of photon attenuation by the head-holder was evaluated by examining the differences in ROI counts in the emission image, attenuation-corrected with and without the head-holder (Table 3). As expected, the head-holder had the maximum effect in the posterior region of the head, which was closest to the head-holder. By including the head-holder in nonuniform attenuation correction, the counts in the occipital ROI improved by ~2%, whereas the frontal region, away from the head-holder, was even more negligibly affected by the head-holder.

Human Studies with Emission and Transmission Imaging

The first reconstruction parameter that we examined was the influence of the placement of the ellipse used for uniform attenuation correction. The emission images were reconstructed with filtered backprojection and attenuation corrected in three different ways using:

1. Uniform attenuation correction with ellipses drawn in the emission image relying on five ^{99m}Tc point markers. These five markers (3 mm^2, each with 5 μCi ^{99m}Tc) were glued to the skin of the head along the canthomeatal line (two on right; three on left);
2. Uniform attenuation correction with ellipses drawn on the attenuation map; and
3. Nonuniform attenuation correction.

The attenuation ellipses drawn on the emission image were typically smaller than those drawn on the attenuation map, except for those slices where the markers were visible on the emission image. The major and minor axes of the ellipses
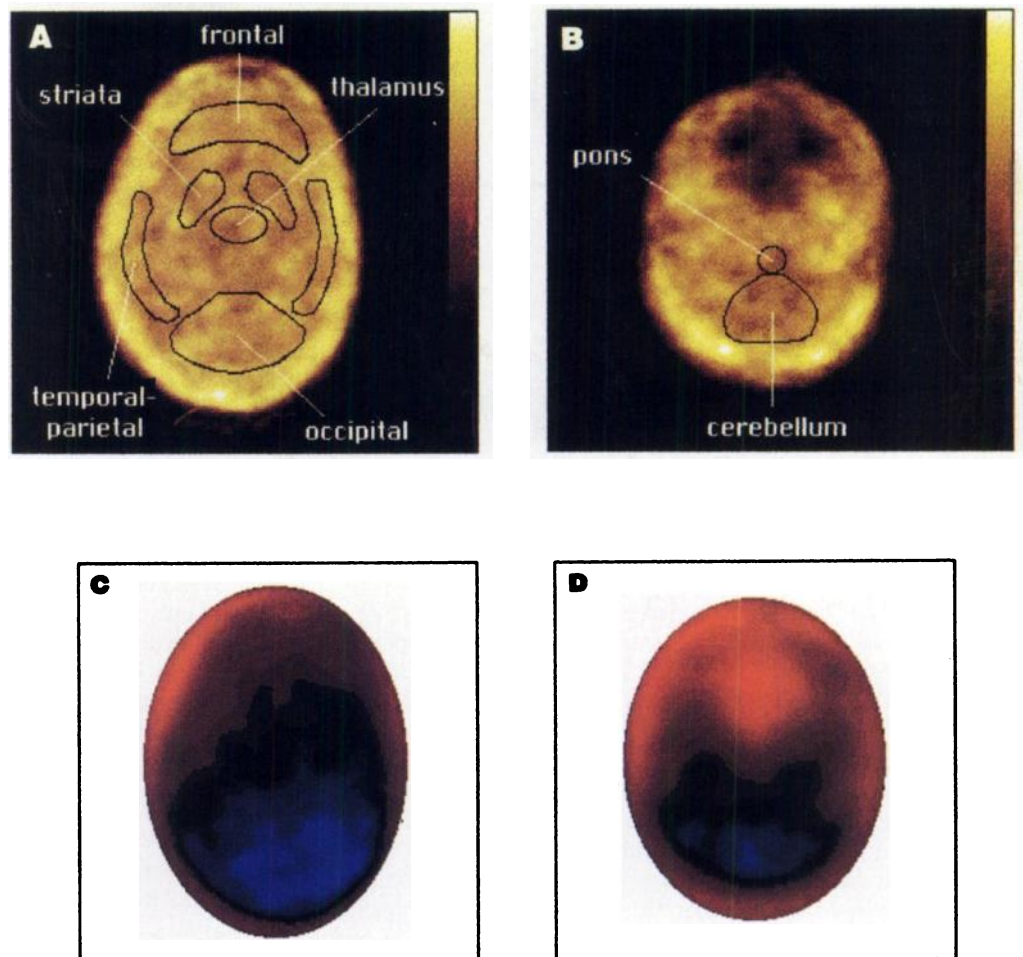
FIGURE 3. Reconstructed attenuation map and image of spatially varying differences in correction factors for uniform and nonuniform attenuation correction. Shown are the attenuation map (A) through the striata and (B) cerebellum and pixel-by-pixel image of difference in attenuation correction factors with uniform and nonuniform attenuation correction through (C) striata and (D) cerebellum. Regions in red indicate overcorrection, and regions in blue imply undercorrection.

TABLE 1
Region of Interest Analysis of Attenuation Correction Factors with Uniform and Nonuniform Attenuation Maps in Healthy Human Subjects

	% Difference in attenuation correction factors for uniform relative to nonuniform attenuation maps*			
	Individual subject		Group of subjects	
Region of interest	% Difference	s.d.	% Difference	s.d.
Striata	−4.33	3.25	−6.42	4.97
Thalamus	−6.21	4.50	−7.84	4.44
Frontal	−2.47	2.48	−4.29	5.55
Occipital	−14.27	3.28	−15.95	6.07
Temporal–parietal	−5.35	2.70	−6.84	4.78
Midbrain	−4.29	2.62	−6.29	7.86
Cerebellum	−11.41	6.27	−13.17	7.97
Pons	−2.49	5.22	−4.42	7.61
Ethmoid sinus	45.21	5.57	44.65	7.38

Nine healthy subjects had transmission-only imaging, and regions of interest (ROIs) were placed on the resulting attenuation maps. The attenuation correction factor is the value (calculated from both the uniform and nonuniform maps) that would be multiplied by the activity in the emission ROI to perform attenuation correction.
*% difference = 100 × (uniform correction factor − nonuniform correction factor)/nonuniform correction factor.

placed on the emission image were 90.3% ± 5.5% and 87.9% ± 5.4%, respectively, of those from the ellipses placed on the transmission image (n = 13 subjects). Thus, uniform attenuation with ellipses drawn in the emission image underestimated activity because of difficulty in determining the proper edge for the ellipse (i.e., the skin).

To compare the absolute quantitation of activity in different ROIs in the brain for the three attenuation correction methods, we calculated the regional %ID in these ROIs by multiplying the concentration of activity by the known volume and then normalizing for the injected dose (Table 4). Uniform attenuation with the ellipse drawn on the attenuation map produced an error of ~5% compared to nonuniform attenuation for striatum, midbrain, thalamus, occipital and cerebellum. However, if the ellipse was drawn on the emission image, the corresponding error was 10%–17%. As expected, these errors were similar for patients and healthy subjects.

Note that the percentage difference between uniform (with ellipse drawn on the attenuation map) and nonuniform attenuation correction is lower in Table 4 than in Table 1. The difference between these two analyses is that Table 4 shows the difference in attenuation-corrected emission counts, whereas Table 1 is the difference in attenuation correction factors (assuming that the emission distribution is uniform within the ROI). However, the distribution of counts in an ROI in the emission image of the human subject varies, resulting in a diminished difference between uniform and nonuniform attenuation correction, when the correction factor is multiplied by

TABLE 2
Recovered Activity in Uniform Attenuation- and Nonuniform Attenuation-Corrected SPECT Images of the Heterogeneous Brain Phantom

	True activity (μCi/cm^3)	Uniform attenuation correction		Nonuniform attenuation correction	
		μCi/cm^3	% error	μCi/cm^3	% error
Left striata	6.40	6.77	5.7	6.36	−0.6
Right striata	6.40	6.82	6.6	6.45	0.7
Background	0.32	0.33	2.2	0.32	−0.6
Left striata/right striata	1.0	0.99	−0.8	0.99	−1.3
Left striata/background	19.2	20.9	8.8	20.0	4.2
Right striata/background	19.2	20.9	8.7	20.3	5.6

the emission intensity. To verify this, a phantom filled with uniform activity was imaged and analyzed two different ways, as in Tables 1 and 4. It was seen that these two analyses gave similar differences between uniform and nonuniform attenuation correction.

The results from ^{123}I-β-CIT SPECT scans are typically expressed as a ratio of target-to-background activity and calculated as (target − background)/background and designated V_3''. The occipital ROI was used as a measure of background uptake, and target regions were identified in striatum, midbrain and thalamus (Table 5). The V_3'' values for these healthy control subjects and Parkinson's disease patients were similar to those reported in larger sized groups (14).

The values of V_3'' for the two methods of uniform attenuation correction (i.e., ellipse placed on either the emission or the transmission image) were very similar to those using nonuniform attenuation correction. Thus, normalization to a background region that shows similar errors of activity measurement to that in the target region effectively compensates for these errors. As a consequence, the relative differences between the values in Parkinson's disease patients compared to healthy control subjects were virtually identical with these three methods. The emission images were also analyzed with no attenuation correction at all. The percentage losses of target ROI values in patients versus healthy control subjects were almost identical to those from the three attenuation-corrected images, both in terms of the percentage loss and the s.d. of these losses. Thus, this limited patient sample suggests that, if SPECT ^{123}I-β-CIT imaging is used primarily to distinguish patient values from those in healthy control subjects, attenuation correction of the images does not add significant diagnostic sensitivity or accuracy for a normalized outcome measure, such as V_3''.

DISCUSSION

Major Findings

The results of this study indicate that quantitative accuracy of SPECT images can be improved significantly by applying nonuniform attenuation correction instead of a uniform method

TABLE 3
Effect of Head-Holder

ROI	Counts in region of interest (ROI) in nonuniform attenuation-correction emission image		
	Head-holder included	Head-holder excluded	% difference
Striata	213.0	212.3	0.33
Midbrain	216.4	215.8	0.28
Frontal	203.8	203.9	0.05
Occipital	215.2	211.1	1.91
Temporal-parietal	208.3	206.7	0.77

using a single average attenuation coefficient. The major sources of error in uniform attenuation correction were the use of an inaccurate uniform attenuation coefficient and improper drawing of the attenuation ellipse.

Without transmission imaging, drawing of the attenuation ellipse is highly prone to errors. Markers are often used in clinical research to identify the head boundary. Markers are useful in only a few cross-sectional slices where they are visible. Drawing the ellipses around the attenuation map produced a 10% improvement in accuracy. In cases in which transmission imaging is not a viable option, the use of scatter windows to obtain an approximate object boundary could be adapted to brain SPECT imaging, as is successfully used in cardiac SPECT imaging for delineating the lung boundaries (19).

Scatter Correction

The purpose of this study was to examine the impact of uniform and nonuniform attenuation correction on emission brain images. However, contamination of measurement data due to scattered photons is also a major source of inaccuracy in quantitative SPECT imaging (20). Here, we have used a simple method for scatter correction by linearly scaling down the nonuniform attenuation values. More sophisticated and accurate methods of scatter correction could, theoretically, have been applied to the current dataset. However, the same simple method of scatter correction was applied to both uniform and nonuniform attenuation correction methods to assess the impact of the attenuation correction methods themselves.

Use of Nonuniform Attenuation as Gold Standard

In the comparison of attenuation correction methods, we have used nonuniform attenuation correction as the gold standard. Although the physics and studies in cardiac SPECT imaging (7,12) strongly suggest nonuniform attenuation correction as an important component in achieving quantitative accuracy, its implementation using the Chang first-order algorithm is not the best-known method. For better accuracy, nonuniform attenuation correction should be implemented as an integral part of iterative algorithms. Nevertheless, the phantom experiments in this study demonstrate a reasonable accuracy for the nonuniform attenuation methods used in this study and suggest that the basic results will be upheld when more sophisticated and computational intensive methods are used.

Impact on Clinical Studies

The results of this study showed that nonuniform attenuation correction produced a modest improvement in absolute quantitation of brain SPECT images compared to uniform attenuation correction when the latter is performed using an ellipse accurately placed on the transmission image. However, in routine clinical brain SPECT imaging, the attenuation ellipse is drawn on the emission image. In the current dataset, the emission images had markers on the skin to help guide the placement of

TABLE 4
Comparison of Attenuation Correction Methods in Measurement of Percentage Injected Dose in Brain Regions of Interest of Healthy and Parkinson Disease Subjects

Subject	ROI	Nonuniform attenuation correction (%ID ± s.d.)	Transmission ellipse %ID ± s.d.	Transmission ellipse % difference*	Emission ellipse %ID ± s.d.	Emission ellipse % difference*
PD	Left striata	0.69 ± 0.17	0.66 ± 0.16	−4.8	0.58 ± 0.14	−16.6
HC	Left striata	1.07 ± 0.24	1.02 ± 0.24	−5.1	0.91 ± 0.22	−15.1
PD	Right striata	0.71 ± 0.22	0.68 ± 0.20	−4.5	0.61 ± 0.18	−15.0
HC	Right striata	1.05 ± 0.24	1.01 ± 0.25	−4.1	0.90 ± 0.22	−14.3
PD	Midbrain	0.43 ± 0.07	0.41 ± 0.07	−4.5	0.36 ± 0.06	−15.7
HC	Midbrain	0.43 ± 0.11	0.41 ± 0.11	−4.4	0.37 ± 0.11	−15.1
PD	Thalamus	0.44 ± 0.11	0.42 ± 0.10	−5.5	0.37 ± 0.08	−16.0
HC	Thalamus	0.48 ± 0.11	0.45 ± 0.11	−5.0	0.41 ± 0.11	−14.1
PD	Occipital	0.20 ± 0.04	0.19 ± 0.04	-4.9	0.17 ± 0.03	−17.2
HC	Occipital	0.16 ± 0.03	0.16 ± 0.03	−4.3	0.14 ± 0.02	−14.8
PD	Cerebellum	0.15 ± 0.04	0.15 ± 0.04	0.0	0.14 ± 0.03	−11.1
HC	Cerebellum	0.11 ± 0.02	0.12 ± 0.02	1.8	0.10 ± 0.02	−10.6

*Percentage difference in %ID with uniform and nonuniform attenuation correction.
ROI = region of interest; HC = healthy control subject; PD = patient with Parkinson's disease.

the ellipse. Despite this extra aid, the uniform attenuation corrected image had errors of 11%–16% for brain regions that were examined.

Analysis using relative measures, such as V_3'' [(specific − nonspecific)/nonspecific], in receptor imaging studies produced only small improvements when attenuation correction was applied to emission images. In such studies (e.g., diagnosis of Parkinson's disease from striatal-to-occipital ratios), nonuniform attenuation correction may not be required.

Transmission imaging and reconstruction of nonuniform attenuation map has an added advantage in brain imaging. The attenuation map can easily be coregistered with an MRI taken on the subject. Coregistration of SPECT with MRIs can be difficult for tracers that have a highly localized uptake and do not provide cortical contours, such as ^{123}I-β-CIT. If transmission imaging is performed either simultaneously with emission imaging or sequentially with no patient movement between the transmission and emission scans, the attenuation map and SPECT image are coregistered intrinsically. The MRIs and transmission images can be coregistered, and the same transformation matrix can then be applied to the emission image.

CONCLUSION

This study suggests that transmission imaging and nonuniform attenuation correction of brain SPECT images should be performed if absolute quantitation of radioligand distribution in the brain is required. However, in some situations in which the outcome measure is a ratio of activities in two brain regions (such as ^{123}I-β-CIT imaging of the dopamine transporter), the improvement in accuracy by nonuniform attenuation correction over uniform attenuation correction is small.

TABLE 5
Influence of Attenuation Correction Method on Specific-to-Nonspecific Binding Ratio Measurements in Healthy and Parkinson's Disease Subjects

ROI	Subjects	Nonuniform attenuation correction Average V_3''	Nonuniform attenuation correction Group COV (%)	Trans-Ellipse Average V_3''	Trans-Ellipse Group COV (%)	Emis-Ellipse Average V_3''	Emis-Ellipse Group COV (%)	No attenuation correction Average V_3''	No attenuation correction Group COV (%)
Left striata	HC	5.70	24.29	5.63	24.36	5.65	22.72	5.11	23.67
	PD	2.41	26.03	2.42	25.82	2.42	25.99	2.11	25.54
	PD vs. HC	−57.77%		−56.97%		−57.07%		−58.68%	
Right striata	HC	5.54	23.66	5.54	23.91	5.56	23.64	4.96	25.30
	PD	2.51	34.22	2.54	33.79	2.61	33.56	2.22	34.19
	PD vs. HC	−54.65%		−54.09%		−53.15%		−55.22%	
Midbrain	HC	1.70	39.10	1.70	39.65	1.67	39.89	1.32	37.78
	PD	1.12	16.16	1.13	15.82	1.15	13.43	0.84	19.70
	PD vs. HC	−34.35%		−33.39%		−31.04%		−35.79%	
Thalamus	HC	2.01	39.15	1.97	39.91	2.01	38.12	1.56	40.70
	PD	1.16	21.89	1.15	21.94	1.20	22.39	0.87	21.92
	PD vs. HC	−42.37%		−41.69%		−40.59%		−44.71%	

ROI = region of interest; V_3'' = specific-to-nonspecific binding ratio; COV = coefficient of variance; HC = healthy control; PD = subject with Parkinson's disease; PD vs. HC = percentage difference in V_3'' between PD and HC subjects, an indicator of PD severity.

REFERENCES

1. Tsui BMW, Gullberg GT, Edgerton ER, et al. Correction of nonuniform attenuation in cardiac SPECT imaging. *J Nucl Med* 1989:30;497-507.
2. Chang LT. A method for attenuation correction in radionuclide computed tomography. *IEEE Trans Nucl Sci* 1978:25;638-643.
3. Gullberg GT, Budinger TF. The use of filtering methods to compensate for constant attenuation in single-photon emission computed tomography. *IEEE Trans Biomed Eng* 1981:28;142-157.
4. Tretiak O, Metz C. The exponential radon transform. *SIAM J Appl Math* 1980:39; 341-354.
5. Murase K, Tanada S, Sugawara Y, Hamamoto K. Improvement of brain single photon emission tomography (SPET) using transmission data acquisition in a four-headed SPET scanner. *Eur J Nucl Med* 1993:20;32-38.
6. Rajeevan N, Penney BC, King MA. Quantitative SPECT imaging: compensation for nonuniform attenuation, scatter, and detector divergence. *Proc IEEE Nucl Sci Symp Med Imag Conf* 1992:2;995-997.
7. Rajeevan N, Penney BC, King MA. Improving the quantitative accuracy and resolution of thoracic SPECT imaging. *Proc IEEE Nucl Sci Symp Med Imag Conf* 1993:2;1345-1348.
8. Tung CH, Gullberg GT, Zeng GL, Christian PE, Datz FL, Morgan HT. Nonuniform attenuation correction using simultaneous transmission and emission converging tomography. *IEEE Trans Nucl Sci* 1992:39;1134-1143.
9. Bettinardi V, Gilardi MC, Cargnel S, Rizzo G, Teräs M, Striano G. A hybrid method of attenuation correction for positron emission tomography brain studies. *Eur J Nucl Med* 1994:21;1279-1284.
10. Turkington TG, Gilland DR, Jaszczak RJ, Greer KL, Coleman RE. A direct measurement of skull attenuation for quantitative SPECT. *IEEE Trans Nucl Sci* 1993:40;1158-1161.
11. Kemp BJ, Prato FS, Nicholson RL, Reese L. Correction for attenuation in technetium-99m-HMPAO SPECT brain imaging. *J Nucl Med* 1992:33;1875-1880.
12. Frey EC, Tsui BMW, Perry JR. Simultaneous acquisition of emission and transmission data for improved thallium-201 cardiac SPECT imaging using a technetium-99m transmission source. *J Nucl Med* 1992:33;2238-2245.
13. Jaszczak RJ, Gilland DR, Jang S, Greer KL, Coleman RE. Fast transmission CT for determining attenuation maps using a collimated line source, rotatable air-copper lead attenuators and fanbeam collimation. *J Nucl Med* 1993:34;1577-1586.
14. Seibyl JP, Marek KL, Quinlan D, et al. Decreased SPECT [^{123}I]β-CIT striatal uptake correlates with symptom severity in idiopathic Parkinson's disease. *Ann Neurol* 1995:38;589-598.
15. Laruelle M, Baldwin RM, Malison RT, et al. SPECT imaging of dopamine and seratonin transporters with [^{123}I]β-CIT: pharmacological characterization of brain uptake in nonhuman primates. *Synapse* 1993:13;295-309.
16. Lange K, Carson RE. EM reconstruction algorithms for emission and transmission tomography. *J Comput Assist Tomogr* 1984:8;306-316.
17. Geman S, McClure DE. Bayesian image analysis: an application to single-photon emission tomography. In: *Proceedings of the Statistical Computer Section, American Statistical Association*, Washington, DC. 1985:12-18.
18. Fahn S, Elton R, Members of the UPDRS development committee. Unified Parkinson's disease rating scale. In: *Recent developments in Parkinson's disease*. Florham Park, NJ: Macmillan Healthcare Information; 1987:153-164.
19. Pan TS, King MA, Penney BC, Rajeevan N, Luo DS, Case JA. Reduction of truncation artifacts in fanbeam transmission by using parallel beam emission data. *IEEE Trans Nucl Sci* 1995:42;1310-1320.
20. Rosenthal MS, Cullom J, Hawkins W, Moore SC, Tsui BMW, Yester M. Quantitative SPECT imaging: a review and recommendations by the focus committee of the Society of Nuclear Medicine computer and instrumentation council. *J Nucl Med* 1995:36; 1489-1513.

FIRST IMPRESSIONS
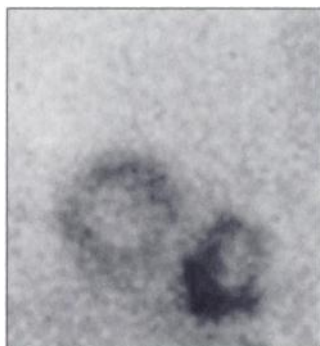## Thallium-201 Imaging of the Myocardium
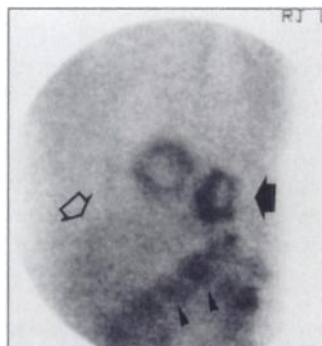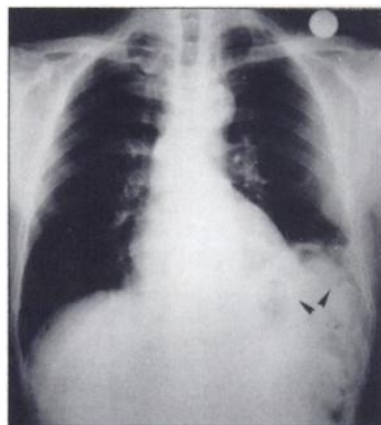

Figure 1.

Figure 2.

Figure 3.

PURPOSE

A 49-yr-old man with existing myocardial infarction underwent treadmill exercise using ^{201}Tl scintigraphy for investigation of the cause of recent onset of chest pain, which usually began after he ate a rich meal. Defects on the septum and inferior walls were seen on the stress images. On the 4-hr redistribution images, minimal improvement in the inferior wall was noted. A reinjection of ^{201}Tl was given, and reimaging was done 18 hr later [Fig. 1, left anterior oblique (LAO) view] for assessment of the viability of the involved walls. The right chamber represents the left colic flexure [Fig. 2, LAO view, 18 hr after reinjection, liver (open arrow), transverse colon (arrowheads) and left colic flexure (thick arrow)]. On the chest radiograph, (Fig. 3) elevation of the hemidiaphragm drawing the left colic flexure up (arrowheads) can be seen.

TRACER
Thallium-201-chloride, 111 MBq (injection) plus 55 MBq (reinjection)

ROUTE OF ADMINISTRATION
Intravenous

TIME AFTER INJECTION
22 hr after injection, 18 hr after reinjection

INSTRUMENTATION
General Electric Starcam 3200 left field-of-view camera with a LEAP collimator

CONTRIBUTORS
G.C. Panoutsopoulos, C. Batsakis, J. Christacacopoulou, Department of Nuclear Medicine, The Athens Chest Hospital, Athens, Greece